

A visible light water-splitting cell with a photoanode formed by codeposition of a high-potential porphyrin and an iridium water-oxidation catalyst†

Gary F. Moore, James D. Blakemore, Rebecca L. Milot, Jonathan F. Hull, Hee-eun Song, Lawrence Cai, Charles A. Schmuttenmaer,* Robert H. Crabtree* and Gary W. Brudvig*

Received 13th January 2011, Accepted 15th April 2011

DOI: 10.1039/c1ee01037a

A high-potential porphyrin is codeposited on TiO₂ nanoparticles together with our Cp*–iridium water-oxidation catalyst to give a photoanode for a water-splitting cell. The photoanode optically resembles the porphyrin yet electrochemically responds like the Ir catalyst when it is immersed in aqueous solutions. Photoelectrochemical data show that illumination of the codeposited anode in water results in a marked enhancement and stability of the photocurrent, providing evidence for light-induced activation of the catalyst.

1. Introduction

Geopolitical issues and environmental concerns emphasize the need for clean, secure, non-fossil energy sources.^{1–7} Solar energy collection and storage is one of the most promising lines for development. In this context, a biomimetic approach offers hope.^{8–11} Many advances in the field of ‘artificial photosynthesis’, including mimicry of energy transfer and charge separation^{12–18} and development of energy-storage catalysis,^{19–32} have been reported. In addition, sensitization of metal-oxide wide band-gap semiconductor surfaces with inorganic transition-metal complexes or organic dyes has been actively pursued in developing methods for converting solar energy to electricity by dye-sensitized solar cells.^{33,34} A promising direction

in this field is the use of semiconductors and dye-sensitized semiconductors as a platform for coupling photochemical charge separation with catalysis.^{35–39} Photoexcitation of a selected sensitizer on n- or p-type semiconductor electrodes will generate an initial charge-separated state that can be used to study subsequent hole or electron transfer to anodic or cathodic catalysts. Practical application of this integrated approach will ultimately require effective coupling of light capture, photochemical charge separation and efficient catalysis.

Herein, we report the optical and electronic properties of a high-potential porphyrin photoanode codeposited with a structural analog of our water-oxidation catalyst (Chart 1).^{30,32} The zinc porphyrin (**1**) and iridium catalyst (**2**) each contains a carboxylic acid group for attachment to TiO₂ nanoparticles (see the ESI†, Experimental procedures). In the catalytic complex, strongly donating ligand sets stabilize the needed high oxidation states of iridium. For the porphyrin dye, bis-pentafluorophenyl electron-withdrawing groups induce an electron deficiency that leads to a positive shift of the porphyrin radical cation/porphyrin redox couple to values that

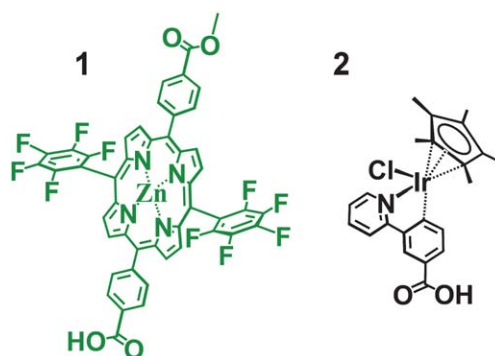


Chart 1 Compounds 1 and 2.

Department of Chemistry, Yale University, P.O. Box 208107, New Haven, CT, 06520-8107, USA. E-mail: g.moore@yale.edu; charles.schmuttenmaer@yale.edu; robert.crabtree@yale.edu; gary.brudvig@yale.edu

† Electronic supplementary information (ESI) available: Experimental, synthesis, NMR, mass spectroscopy, optical and electrochemical data, and X-ray crystal structure of Cp*IrCl(3'-carboxy-2-phenylpyridine). See DOI: 10.1039/c1ee01037a

Broader context

Artificial photosynthesis is a long-sought goal in solar energy research. By splitting water into O₂ and a fuel such as H₂, two problems are addressed: energy storage and the production of a potential transport fuel. This communication describes a water splitting photocell that uses a specially designed photoanode to which are attached both a high potential porphyrin dye for light absorption and a Cp*–iridium catalyst for water oxidation. The cell is completed by a standard Pt cathode.

permit water oxidation. Illumination of these photoanodes in complete cells results in a marked enhancement and stability of the photocurrent for electrodes in water, consistent with light-induced activation of the catalyst.

2. Results and analysis

2.1 Electrochemical characterization

The 10,20-bis(pentafluorophenyl) groups of **1** have a strong influence on the electrochemical properties of the porphyrin ring system as the electron-withdrawing nature of these functional groups destabilizes the formation of the radical-cation species.^{40,41} For dichloromethane solutions of the methyl ester of porphyrin (**1**), the first and second oxidations of the porphyrin are chemically reversible and occur with an $E_{1/2}$ of 1.35 and 1.59 V vs. NHE, respectively (see the ESI†, Fig. S7). Thus, the oxidized porphyrin species (**1**⁺) is thermodynamically capable of water oxidation (yet kinetically ineffective on its own).

We have previously reported the catalytic performance of a homogeneous Cp*Ir water oxidation catalyst in a mixed-solvent solution (acetonitrile–water mixture) with Ce(IV) as the primary oxidant.^{30,32} Now, we report a close analogue (**2**) bearing a carboxylic acid group for surface attachment to TiO₂. Cyclic voltammograms of **2** deposited on a TiO₂-sintered FTO working electrode (**2-TiO₂**) in 0.1 M Na₂SO₄ exhibit an increase of anodic currents at potentials positive of 1 V vs. NHE (Fig. 1, left). These results indicate that immobilization of the catalyst onto the electrode surface allows operation under aqueous conditions when the required potentials are applied. Rotating electrode (RRDE) measurements (see the ESI†, Fig. S10) confirm that oxygen can be formed at the surface of a sintered TiO₂ Pt-disc electrode functionalized with **2**. Further, electrodes codeposited with **1** and **2** (**1 + 2-TiO₂**) maintain the catalytic feature observed in cyclic voltammograms of TiO₂ on FTO electrodes treated solely with **2**, a crucial feature for deployment in photocatalytic-electrochemical cells. The overall current density is,

however, significantly lower in the codeposited material; some diminution may be expected, as the presence of porphyrin sensitizers limits the surface area available for catalyst deposition. Cyclic voltammograms of the unfunctionalized TiO₂-sintered FTO working electrode, as well as electrodes treated only with **1**, are included in Fig. 1; neither gives rise to the increased anodic currents observed for electrodes treated with **2**. The surface loadings for **1-TiO₂** and **2-TiO₂** as determined by quantitative mass spectrometry (see the ESI†, Experimental procedures) are 3.4×10^{-8} and 7.6×10^{-8} mol cm⁻², respectively.

2.2 Optical characterization

The spectral features of the codeposited material (**1 + 2-TiO₂**) (Fig. 1, right) are dominated by the porphyrin due to its relatively high molar extinction coefficient (see the ESI†, Fig. S7). Likewise, the porphyrin dye extends the absorption of the anode well into the visible region. Thus, the codeposited anode is optically more similar to **1-TiO₂** yet electrochemically responds like **2-TiO₂** in aqueous solutions. The intersection of the normalized absorption and emission spectra of compound **1** in dichloromethane yields an estimated $E^{0,0}$ transition energy of ~ 2.12 eV (see the ESI†, Fig. S8). The estimated potential for the excited-state couple (E^0 (**1**⁺/**1**^{*}) ≈ -0.77 V vs. NHE) is negative of the TiO₂ conduction band (TiO₂ CB ≈ -0.57 V vs. NHE).⁴² Thus, **1**^{*} should be energetically capable of injecting electrons into the conduction band of TiO₂ and photochemically generating the **1**⁺ radical-cation species at the surface.

2.3 Time-resolved terahertz measurements

Interfacial electron-transfer dynamics of functionalized metal-oxide nanoparticle thin films were studied with subpicosecond temporal resolution by time-resolved terahertz spectroscopy (see the ESI†, Experimental procedures). Results obtained for a 400 nm optical pump/THz probe of TiO₂ colloidal nanoparticle thin films, including unfunctionalized as well as **1-TiO₂**, **2-TiO₂**, and **1 + 2-TiO₂**, are

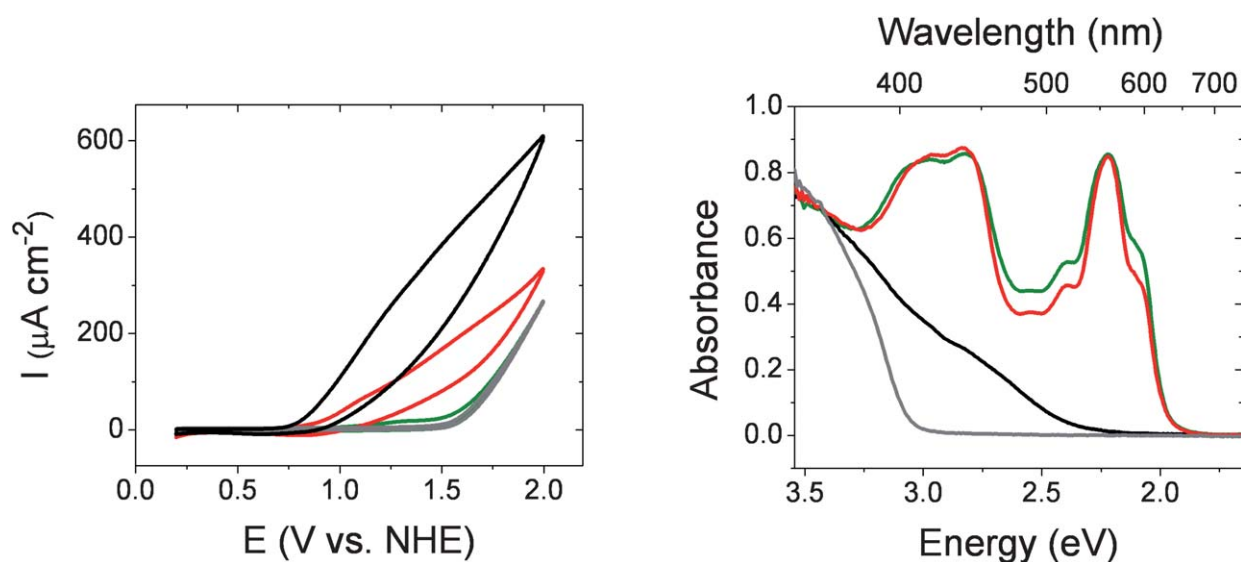


Fig. 1 Cyclic voltammograms (left) of TiO₂ (grey), **1-TiO₂** (green), **2-TiO₂** (black), and **1 + 2-TiO₂** (red) deposited on a conductive FTO-coated glass working electrode in water (0.1 M Na₂SO₄) as well as diffuse reflectance spectra (right) of a thin film of TiO₂ (grey), **1-TiO₂** (green), **2-TiO₂** (black), and **1 + 2-TiO₂** (red).

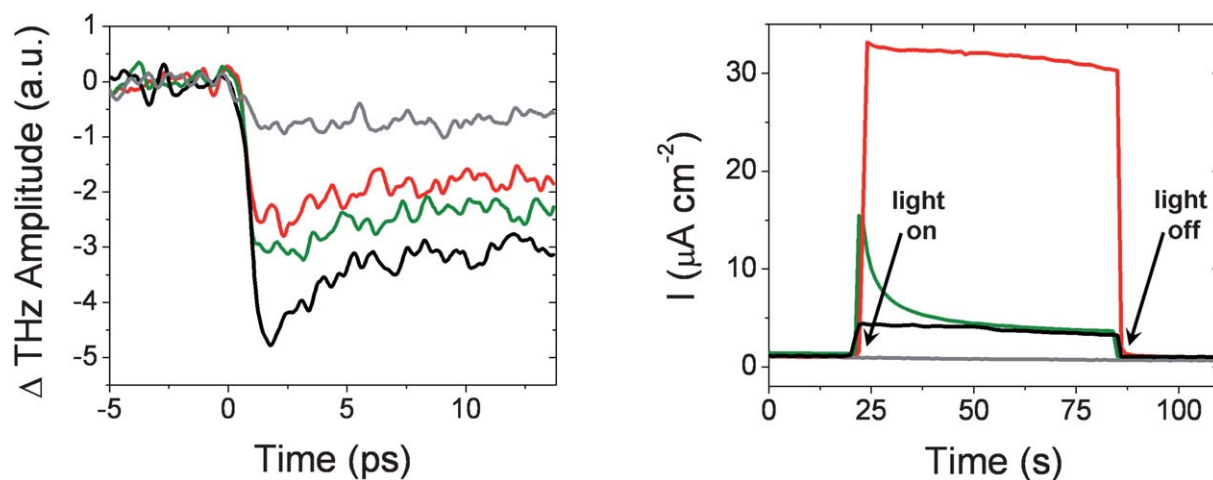


Fig. 2 (left) Time-resolved terahertz probe spectra obtained with a 400 nm optical pump of a thin film of TiO_2 (grey), 1-TiO_2 (green), 2-TiO_2 (black), and $1 + 2\text{-TiO}_2$ (red), and (right) three-electrode photocurrent measurements using a H-cell configuration (see the ESI†, Experimental procedures) with a 0.3 V external bias for TiO_2 (grey), 1-TiO_2 (green), 2-TiO_2 (black), and $1 + 2\text{-TiO}_2$ (red) deposited on conductive FTO-coated glass working electrodes in water (0.1 M Na_2SO_4) upon illumination with a $\sim 200 \text{ mW cm}^{-2}$ white-light source coupled to a 400 nm long-pass filter.

illustrated in (Fig. 2, left). There is negligible change in the THz transmittance of the bare TiO_2 sample, consistent with the negligible absorbance at 400 nm. Results obtained for 1-TiO_2 indicate effective photoinduced charge injection. These results are consistent with the estimated excited-state potential of **1** versus the more positive potential of the TiO_2 conduction band. Also evident in Fig. 2 is the relatively large change in THz amplitude obtained for thin films of **2** on TiO_2 . Further, the signal obtained for the codeposited film is less intense in comparison with those obtained for films treated only with **1** or **2**, indicating a decrease in the number of electrons which have become mobilized in the TiO_2 conduction band in the first 10 ps after photoexcitation. This decrease in electron injection suggests that the electron injection for the codeposited films is not simply a result of independent electron injection from both **1** and **2** and that the mechanism of electron injection is altered when **1** and **2** are codeposited on the surface of TiO_2 .

2.4 Photocurrent measurements

Photocurrent measurements were conducted with TiO_2 sintered on conductive FTO-coated glass working electrodes in 0.1 M Na_2SO_4 using a three-electrode configuration with a Ag/AgCl reference electrode, a 0.3 V bias potential (see the ESI†, Experimental procedures) and a Pt counter electrode. The anode compartment was separated from the cathode with a coarse glass frit and illuminated with a $\sim 200 \text{ mW cm}^{-2}$ light source (Fig. 2, right). In all experiments, a 400 nm long-pass filter was used to avoid direct band gap excitation of TiO_2 (Fig. 1, right). Thus, illumination of untreated TiO_2 anodes results in negligible photocurrent under these conditions. For porphyrin-sensitized photoanodes lacking the catalyst (1-TiO_2), illumination results in a sharp transient current arising from the initial, yet unsustained, injection of electrons from the photoexcited porphyrin species (1^*). Photocurrent of a similar intensity is observed for catalyst-sensitized photoanodes lacking the porphyrin dye (2-TiO_2). In contrast to these results photoexcitation of codeposited anodes gives rise to a significantly increased and sustained photocurrent (on the seconds timescale) in complete cells,

consistent with the model of visible light-induced activation of the catalyst.

3. Conclusions

Our bioinspired photochemical cell consists of a high-potential porphyrin attached to a TiO_2 surface that is codeposited with an iridium-based water-oxidation catalyst. Our characterization indicates the catalyst remains active on the surface. Photoexcitation of the surface-attached porphyrin generates the porphyrin excited-state species (1^*), which is energetically poised to inject electrons into the conduction band of TiO_2 , forming the relatively high potential porphyrin radical cation (1^+), a species that is thermodynamically capable of acting as a primary oxidant of water.

Time-resolved optical pump/terahertz probe measurements are consistent with our energetic model based on electrochemical and optical data. These measurements allow for a direct non-contact probe of the timescale and efficiency of photoinduced charge injection and recombination or trapping. We have previously found a good correlation between this type of THz measurement and efficiencies of dye-sensitized solar cells.⁴³ However, the present lack of correlation between the THz measurements and photocurrent generation indicates that charge injection on a ps timescale is not the limiting factor in photocurrent generation in complete cells.

Photoexcitation of complete cells, under our conditions (see the ESI†, Experimental procedures), gives rise to a photocurrent that is significantly increased and sustained in comparison with results obtained in control experiments lacking any one component of the complete cell. These results are consistent with our working model of the sustained current arising from light activation of the catalyst resulting from the transport of holes from photooxidized porphyrin dyes and/or possible migration of holes from other oxidized iridium sites. Our photocurrents ($\sim 30 \mu\text{A cm}^{-2}$) compare favorably to those in prior work,^{36,38} but we do need a bias voltage, as in one prior case.³⁶ A bias voltage was avoided in the work of Brimblecombe *et al.*,³⁸ but UV irradiation was employed. In a future full paper, we aim to provide quantitative efficiency data on the basis of a better

understanding of the loading of the components and the oxygen output of the cell.

Acknowledgements

This work was supported by the Office of Basic Energy Sciences of the U.S. Department of Energy (DE-FG02-07ER15909 and DE-FG02-84ER13297) and the Camille & Henry Dreyfus Foundation. The authors acknowledge Nathan D. Schley and Christopher D. Incarvito for their efforts in obtaining the X-ray crystal structure of Cp*IrCl(3'-carboxy-2-phenylpyridine).

References

- 1 IPCC, 2007: *Summary for Policy Makers*, Cambridge University Press, Cambridge, United Kingdom and New York, NY, USA, 2007.
- 2 *Directing Matter and Energy: Five Challenges for Science and the Imagination*, U.S. Dep. Energy, Washington, DC, December, 2007.
- 3 *New Sciences for a Secure and Sustainable Energy Future*, U.S. Dep. Energy, Washington, DC, December, 2008.
- 4 *Basic Research Needs: Catalysis For Energy*, U.S. Dep. Energy, Washington, DC, August, 2007.
- 5 *International Energy Outlook 2009*, U.S. Dep. Energy, Washington, DC, May, 2009.
- 6 M. I. Hoffert, K. Caldeira, A. K. Jain, E. F. Haites, L. D. D. Harvey, S. D. Potter, M. E. Schlesinger, S. H. Schneider, R. G. Watts, T. M. L. Wigley and D. J. Wuebbles, *Nature*, 1998, **395**, 881–884.
- 7 N. S. Lewis and D. G. Nocera, *Proc. Natl. Acad. Sci. U. S. A.*, 2006, **103**, 15729–15735.
- 8 J. P. McEvoy and G. W. Brudvig, *Chem. Rev.*, 2006, **106**, 4455–4483.
- 9 M. Hambourger, G. F. Moore, D. M. Kramer, D. Gust, A. L. Moore and T. A. Moore, *Chem. Soc. Rev.*, 2009, **38**, 25–35.
- 10 I. McConnell, G. Li and G. W. Brudvig, *Chem. Biol.*, 2010, **17**, 434–447.
- 11 G. F. Moore and G. W. Brudvig, *Annu. Rev. Condens. Matter Phys.*, 2011, **2**, 303–327.
- 12 M. R. Wasielewski, *Chem. Rev.*, 1992, **92**, 435–461.
- 13 D. Gust, T. A. Moore and A. L. Moore, *Acc. Chem. Res.*, 1993, **26**, 198–205.
- 14 D. Gust, T. A. Moore and A. L. Moore, *Acc. Chem. Res.*, 2001, **34**, 40–48.
- 15 D. Gust, T. A. Moore and A. L. Moore, *Acc. Chem. Res.*, 2009, **42**, 1890–1898.
- 16 L. Hammarström, *Curr. Opin. Chem. Biol.*, 2003, **7**, 666–673.
- 17 T. J. Meyer, *Acc. Chem. Res.*, 1989, **22**, 163–170.
- 18 S. Fukuzumi, *Phys. Chem. Chem. Phys.*, 2008, **10**, 2283–2297.
- 19 A. Harriman, I. J. Pickering, J. M. Thomas and P. A. Christensen, *J. Chem. Soc., Faraday Trans. 1*, 1988, **84**, 2795–2806.
- 20 W. Ruettinger and G. C. Dismukes, *Chem. Rev.*, 1997, **97**, 1–24.
- 21 R. Manchanda, G. W. Brudvig and R. H. Crabtree, *Coord. Chem. Rev.*, 1995, **144**, 1–38.
- 22 C. W. Cady, R. H. Crabtree and G. W. Brudvig, *Coord. Chem. Rev.*, 2008, **252**, 444–455.
- 23 M. Yagi and M. Kaneko, *Chem. Rev.*, 2001, **101**, 21–35.
- 24 J. L. Dempsey, B. S. Brunschwig, J. R. Winkler and H. B. Gray, *Acc. Chem. Res.*, 2009, **42**, 1995–2004.
- 25 A. J. Morris, G. J. Meyer and E. Fujita, *Acc. Chem. Res.*, 2009, **42**, 1983–1994.
- 26 M. Rakowski Dubois and D. L. Dubois, *Acc. Chem. Res.*, 2009, **42**, 1974–1982.
- 27 M. W. Kanan and D. G. Nocera, *Science*, 2008, **321**, 1072–1075.
- 28 A. Le Goff, V. Artero, B. Jousset, P. D. Tran, N. Guillet, R. Metaye, A. Fihri, S. Palacin and M. Fontecave, *Science*, 2009, **326**, 1384–1387.
- 29 F. Jiao and H. Frei, *Angew. Chem., Int. Ed.*, 2009, **48**, 1841–1844.
- 30 J. F. Hull, D. Balcells, J. D. Blakemore, C. D. Incarvito, O. Eisenstein, G. W. Brudvig and R. H. Crabtree, *J. Am. Chem. Soc.*, 2009, **131**, 8730–8731.
- 31 Z. Ning, Y. Fu and H. Tian, *Energy Environ. Sci.*, 2010, **3**, 1170–1181.
- 32 J. D. Blakemore, N. D. Schley, D. Balcells, J. F. Hull, G. W. Olack, C. D. Incarvito, O. Eisenstein, G. W. Brudvig and R. H. Crabtree, *J. Am. Chem. Soc.*, 2010, **132**, 16017–16029.
- 33 B. O'Regan and M. Grätzel, *Nature*, 1991, **353**, 737–740.
- 34 M. Grätzel, *Nature*, 2001, **414**, 338–344.
- 35 A. Fujishima and K. Honda, *Nature*, 1972, **238**, 37–38.
- 36 W. J. Youngblood, S.-H. A. Lee, Y. Kobayashi, E. A. Hernandez-Pagan, P. G. Hoertz, T. A. Moore, A. L. Moore, D. Gust and T. E. Mallouk, *J. Am. Chem. Soc.*, 2009, **131**, 926–927.
- 37 D. K. Zhong, J. Sun, H. Inumaru and D. R. Gamelin, *J. Am. Chem. Soc.*, 2009, **131**, 6086–6087.
- 38 R. Brimblecombe, A. Koo, G. C. Dismukes, G. F. Swiegers and L. Piccia, *J. Am. Chem. Soc.*, 2010, **132**, 2892–2894.
- 39 T. W. Woolerton, S. Sheard, E. Reisner, E. Pierce, S. W. Ragsdale and F. A. Armstrong, *J. Am. Chem. Soc.*, 2010, **132**, 2132–2133.
- 40 G. F. Moore, M. Hambourger, M. Gervaldo, O. G. Poluektov, T. Rajh, D. Gust, T. A. Moore and A. L. Moore, *J. Am. Chem. Soc.*, 2008, **130**, 10466–10467.
- 41 G. F. Moore, M. Hambourger, G. Kodis, W. Michl, D. Gust, T. A. Moore and A. L. Moore, *J. Phys. Chem. B*, 2010, **114**, 14450–14457.
- 42 G. Rothenberger, D. Fitzmaurice and M. Graetzel, *J. Phys. Chem.*, 1992, **96**, 5983–5986.
- 43 G. Li, C. P. Richter, R. L. Milot, L. Cai, C. A. Schmuttenmaer, R. H. Crabtree, G. W. Brudvig and V. S. Batista, *Dalton Trans.*, 2009, 10078–10085.

Supporting Information for

A Visible Light Water-Splitting Cell with a Photoanode formed by Codeposition of a High-Potential Porphyrin and an Iridium Water-Oxidation Catalyst

Gary F. Moore, James D. Blakemore, Rebecca L. Milot, Jonathan F. Hull, Hee-eun Song, Lawrence Cai, Charles A. Schmuttenmaer,* Robert H. Crabtree,* and Gary W. Brudvig*

Department of Chemistry, Yale University, P.O. Box 208107, New Haven, Connecticut 06520-8107

E-mail: g.moore@yale.edu, charles.schmuttenmaer@yale.edu, robert.crabtree@yale.edu,
gary.brudvig@yale.edu

<i>Index</i>	<i>Page</i>
S1. Experimental Procedures	S2-S3
S2. Synthesis and Structural Characterization	S4-S7
S3. Nuclear Magnetic Resonance Spectra	S7-S9
S4. Optical and Electrochemical Data	S7-S12
S5. X-ray Crystal Structure of Cp*IrCl(3'-carboxy-2-phenylpyridine)	S12-S16
S.6. References	S17

S1. Experimental Procedures

All reagents were purchased from Aldrich, Alfa Aesar or Mallinckrodt. Dichloromethane was purified with a solvent purification system (Innovative Technologies, Inc) using a 1-m column containing activated alumina. All solvents were stored over the appropriate molecular sieves prior to use. MilliQ water was used to prepare all of the aqueous solutions.

S1.1. Sample preparation and characterization

All compounds were synthesized from commercially available starting materials (see SI, Synthesis and Structural Characterization). Thin layer chromatography (TLC) was performed with silica gel coated glass plates from EMD Chemicals. Column chromatography was carried out using silica gel 60, 230-400 mesh from EMD Chemicals. NMR spectra were recorded on Bruker spectrometers operating at 400 or 500 MHz. NMR samples were prepared in deuteriochloroform or 1% deuteriopyridine in deuteriochloroform with tetramethylsilane as an internal reference for ^1H -NMR and trichlorofluoromethane as an external reference for ^{19}F -NMR. Mass spectra were obtained with a matrix-assisted laser desorption/ionization time-of-flight spectrometer (MALDI-TOF). Steady-state absorbance spectra were measured on a Varian Cary 300 UV-visible spectrophotometer. Steady-state fluorescence spectra were measured using a Shimadzu RF-5301PC spectrometer.

Photoanodes were prepared in a manner similar to that reported previously.¹ Commercially available P25 TiO_2 nanoparticles were used as received from Degussa (now Evonik). Fluorine-doped tin oxide (FTO) conductive glass slides (Tec 8, visible light transmittance 77 %, Hartford Inc., USA) were rinsed with ethanol before use. Pastes composed of 1.0 g TiO_2 in 2 mL Milli-Q water were stirred overnight to obtain a homogeneous dispersion and then coated by the doctor-blade method onto the FTO glass slides with area 1 to 1.3 cm^2 and thickness $\sim 10 \mu\text{m}$. The electrodes were dried at room temperature and sintered in air at 450 $^\circ\text{C}$ for 2 h with a ramp rate 5 $^\circ\text{C}/\text{min}$. The TiO_2 electrodes were sensitized by soaking the slide in a 0.1 mM solution of porphyrin compound **1**, catalyst compound **2**, or a 1:1 mixture of **1** and **2** (each 0.1 mM in concentration) in 10% ethanol in dichloromethane overnight at room temperature. Following sensitization, the photoanodes were rinsed with 10% ethanol in dichloromethane solution and dried at room temperature.

S1.2 Electrochemical measurements

Cyclic voltammetry was performed with an EG&G Princeton Applied Research Model 273A potentiostat/galvanostat using a glassy carbon (3 mm diameter) or platinum disc (1.6 mm diameter) or FTO working electrode, a platinum counter electrode, and a silver wire pseudoreference electrode or a Ag/AgCl electrode (Bioanalytical Systems, Inc. Ag/AgCl vs. NHE: +197 mV)^{2, 3} in a conventional three-electrode cell. For organic solutions, anhydrous dichloromethane or acetonitrile was used as the solvent. The supporting electrolyte was 0.10 M tetrabutylammonium perchlorate or 0.10 M tetrabutylammonium hexafluorophosphate and the solution was deoxygenated by bubbling with nitrogen. The platinum disc working electrode was cleaned between experiments by polishing with an alumina slurry, followed by solvent rinses. The concentration of the electroactive compound was $\sim 3 \times 10^{-3}$ M. The potential of the pseudoreference electrode was determined using the ferrocenium/ferrocene redox couple as an internal standard (with $E_{1/2}$ taken as 0.690 V vs. NHE in dichloromethane).² For aqueous solutions, the supporting electrolyte was 0.1 M Na_2SO_4 . All reported voltammograms were

recorded at a 100 mV s^{-1} scan rate. All potentials listed in this manuscript are referenced to the normal hydrogen electrode (NHE) unless otherwise stated.

Aqueous rotating ring-disc electrochemistry (RRDE) experiments were carried out with a Pine AFCBP1 Bipotentiostat and a Pine MSR variable-speed rotator. The supporting electrolyte was $0.1 \text{ M Na}_2\text{SO}_4$. The reference was a Ag/AgCl electrode (Bioanalytical Systems, Inc., Ag/AgCl vs. NHE: $+197 \text{ mV}$)^{2, 3} and the counter electrode was a platinum wire. The disc and ring electrode materials were platinum. The platinum disc was prepared with a TiO_2 film in the manner described above by doctor blading and sintering.

S1.1.3. Elemental analysis

All samples were analyzed on a Costech ECS 4010 elemental analyzer (Costech Analytical Technologies, Valencia, CA) coupled to a ThermoFinnigan DeltaPLUS Advantage stable isotope mass spectrometer (Thermo Scientific, Boca Raton, FL), with both controlled by the Thermo's Isodat 2.0 software. In a typical run, a dried TiO_2 sample (0.5–1.0 mg) was sealed in a tin capsule and loaded into the autosampler. Control experiments were run using pure TiO_2 materials and powdered complex **1**, and the results were calibrated with the house standard (standard cocoa powder, 4.15% N; 48.7% C). The output of the elemental analyzer, the N_2 and the CO_2 from N and C on TiO_2 surfaces, was sampled by the mass spectrometer.

S1.4. Reflectance measurements

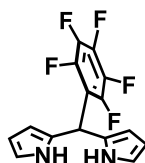
UV/visible spectra were taken on a Varian Cary 300 spectrophotometer with an integrating sphere attachment. Thin films of TiO_2 samples were doctor-bladed on microscope slides and heated to $450 \text{ }^\circ\text{C}$ for 2 h with a ramp rate of $5 \text{ }^\circ\text{C}/\text{min}$. The thin films were then sensitized with porphyrin dye **1** and/or catalyst **2** by soaking in a 10% solution of ethanol in dichloromethane overnight and dried at room temperature before collecting spectra. The same sensitized films were also used in the THz studies.

S1.5. Time-resolved terahertz spectroscopy measurements

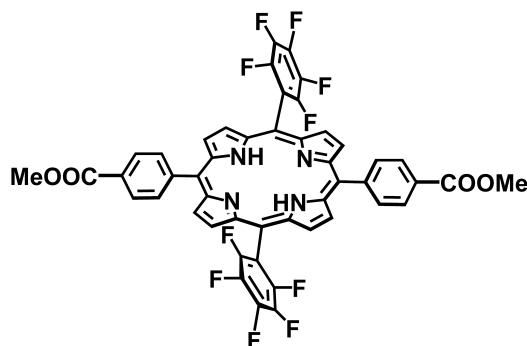
Interfacial electron-transfer dynamics of functionalized metal-oxide nanoparticle thin films were studied, with subpicosecond temporal resolution, using time-resolved terahertz spectroscopy. In these experiments, THz radiation is absorbed by mobile electrons in the metal-oxide conduction band, and the change in THz amplitude is a product of the carrier density and mobility.^{4, 5} Photoexcitation and subsequent electron injection results in an increase of the metal-oxide free-carrier population, decreasing the THz transmission amplitude. Such measurements allow for a direct comparison of the timescale and efficiency of photoinduced charge injection and recombination or trapping. An amplified Ti:sapphire laser (Tsunami/Spitfire from Spectra Physics) generated 800 mW of pulsed near-IR light at a 1 kHz repetition rate. The pulse width was 100 fs, and the center wavelength was 800 nm. Roughly two-thirds of the power was frequency doubled and then filtered to produce 40 mW of 400 nm (3.10 eV) light for the pump beam. The remainder of the near-IR light was used to generate and detect THz radiation. Terahertz radiation was generated using optical rectification in a ZnTe(110) crystal and detected using free-space electro-optic sampling in a second ZnTe (110) crystal. Terahertz data were taken at room temperature using the samples that were prepared for UV/visible measurements, and the average of two samples was taken for each data set. To analyze electron injection

dynamics, the change in THz transmission was monitored as the time delay between the 400-nm pump pulse and the THz probe pulse was varied. Further information on the spectrometer and techniques is reported in the literature.^{4,6}

S2. Synthesis and Characterization:

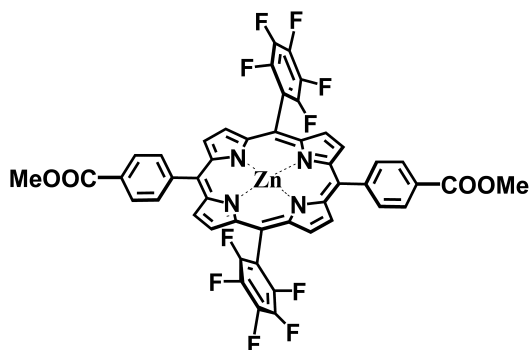


5-(Pentafluorophenyl)dipyrromethane. A similar method was previously reported.⁷ A solution of pentafluorobenzaldehyde (2.0 mL, 16.2 mmol) in freshly distilled pyrrole (50 mL, 720 mmol) was degassed with a stream of argon for 20 min before adding trifluoroacetic acid (120 μ L, 1.62 mmol). The mixture was stirred for 30 min at room temperature, diluted with CH_2Cl_2 (400 mL), and then washed with 0.1M NaOH (400 mL). The organic phase was washed with water (400 mL) and dried over Na_2SO_4 . Evaporation of the solvent at reduced pressure gave brown oil. Unreacted pyrrole was removed under high vacuum, yielding a tacky solid that was flashed on a column of silica using a mixture of hexanes:ethyl acetate:triethylamine (80:20:1) as the eluent. The product was recrystallized from dichloromethane/hexanes to yield 3.29 g of 5-(pentafluorophenyl)dipyrromethane as a white powder (65% yield). ^1H NMR (400 MHz, CDCl_3): δ 5.90 (1H, s, CH), 6.00 – 6.05 (2H, m, ArH), 6.14– 6.19 (2H, m, ArH), 6.71 – 6.75 (2H, m, ArH), 8.06 (2H, brs, NH); ^{19}F NMR (400 MHz, CDCl_3): δ -160.98 – -161.40 (2F, m, ArF), -155.71 (1F, t, $J = 21.0$ Hz, ArF), -141.43 (2F, brd, $J = 20.7$ Hz, ArF).



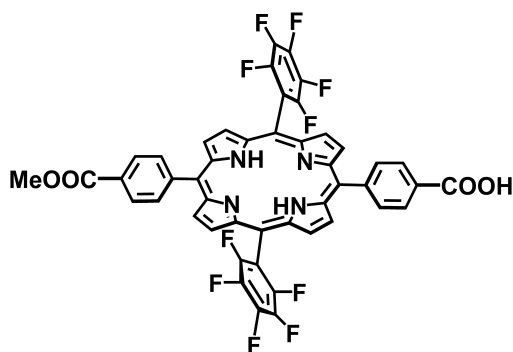
5,15-Bis(4-carbomethoxyphenyl)-10,20-bis(pentafluorophenyl)porphyrin. A portion of 5-(pentafluorophenyl)dipyrromethane (1.15 g, 3.68 mmol), and 4-carbomethoxybenzaldehyde (663 mg, 3.68 mmol) in chloroform (370 mL) was purged for 20 minutes with argon before adding $\text{BF}_3(\text{OEt}_2)$ (486 μ L of a 2.5M stock solution in chloroform). After 24 h, 2,3-dichloro-5,6-dicyano-1,4-benzoquinone (DDQ) (625 mg, 2.75 mmol) was added and the mixture was stirred for an additional 24 h. The solvent was evaporated at reduced pressure and the residue was redissolved in toluene. The solution was treated with a second portion of DDQ (625 mg, 2.75 mmol) and refluxed for 2.5 h. The toluene was removed at reduced pressure and the crude product was purified by column chromatography on silica using chloroform as the eluent. Recrystallization from chloroform/methanol gave 318 mg of the desired porphyrin as a purple

crystalline solid (19% yield). ^1H NMR (400 MHz, CDCl_3): δ -2.86 (2H, s, NH), 4.13 (6H, s, CO_2CH_3), 8.31 (4H, d, $J = 8.1$ Hz, ArH), 8.47 (4H, d, $J = 8.1$ Hz, ArH), 8.83 (4H, d, $J = 4.8$ Hz, βH), 8.91 (4H, d, $J = 4.8$ Hz, βH); ^{19}F NMR (400 MHz, in CDCl_3): δ -161.49 – -161.96 (4F, m, ArF), -151.95 (2F, t, $J = 21.2$ Hz, ArF); -136.81 (4F, dd, $J = 8.1$ Hz, 23.7 Hz, ArF); MALDI-TOF-MS m/z . calcd. for $\text{C}_{48}\text{H}_{24}\text{F}_{10}\text{N}_6\text{O}_4$ 910.164, obsd. 910.169; UV-vis (CH_2Cl_2) 416, 510, 543 587, 641 nm. Emission (CH_2Cl_2) 646, 709 nm.



Zinc 5,15-bis(4-carbomethoxyphenyl)-10,20-bis(pentafluorophenyl)porphyrin.

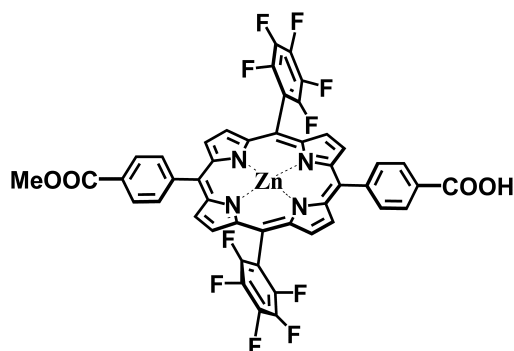
$\text{Zn}(\text{OAc})_2 \cdot 2\text{H}_2\text{O}$ (84 mg, 0.38 mmol) was added to a solution of 5,15-bis(4-carbomethoxyphenyl)-10,20-bis(pentafluorophenyl)porphyrin (35 mg, 0.04 mmol) in a mixture of dichloromethane and methanol (80:20, 50 mL). After stirring for 15 h, the solution was diluted with dichloromethane (25 mL) and washed with water (75 mL), then a saturated solution of aqueous sodium bicarbonate. The organic phase was dried over sodium sulfate, filtered, and the solvent evaporated at reduced pressure. The product was purified by column chromatography on silica using dichloromethane as the eluent to give 37 mg of the desired porphyrin (98% yield). ^1H NMR (500 MHz, 1% Pyridine- d_5 in CDCl_3): δ 4.09 (6H, s, CO_2CH_3), 8.24 (4H, d, $J = 8.3$ Hz, ArH), 8.42 (4H, d, $J = 8.3$ Hz, ArH), 8.87 (4H, d, $J = 4.8$ Hz, βH), 8.90 (4H, d, $J = 4.8$ Hz, βH); ^{19}F NMR (400 MHz, 1% Pyridine- d_5 in CDCl_3): δ -162.68 – -162.49 (4F, m, ArF), -153.29 (2F, t, $J = 20.9$ Hz, ArF); -137.54 (4F, dd, $J = 8.5$ Hz, 24.7 Hz, ArF); MALDI-TOF-MS m/z . calcd. for $\text{C}_{48}\text{H}_{22}\text{F}_{10}\text{N}_6\text{O}_4\text{Zn}$ 927.077, obsd. 927.079 UV-vis (CH_2Cl_2) 415, 545, 578 nm Emission (CH_2Cl_2) 590, 642 nm.



5-(4-Carbomethoxyphenyl)-15-(4-carboxyphenyl)-10,20-bis(pentafluorophenyl)porphyrin.

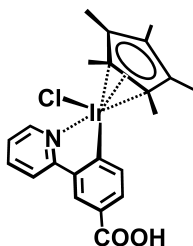
A portion of 5,15-bis(4-carbomethoxyphenyl)-10,20-bis(pentafluorophenyl)porphyrin (100 mg, 0.11 mmol) was dissolved in a mixture of trifluoroacetic acid and conc. HCl (1:2, 80 mL) at 45°

C for 24 h. The reaction mixture was diluted with dichloromethane (80 mL), washed twice with an equal volume of water, and then neutralized with a saturated solution of aqueous sodium bicarbonate. The organic phase was dried over sodium sulfate, filtered, and the solvent removed at reduced pressure. The crude product was purified by column chromatography on silica using a gradient of 1% methanol in dichloromethane to 10% methanol in dichloromethane as the eluent to give 59 mg of the desired porphyrin (60% yield). ^1H NMR (500 MHz, 1% Pyridine-*d*5 in CDCl_3): δ -2.86 (2H, s, NH), 4.11 (3H, s, CO_2CH_3), 8.30 (2H, d, $J = 8.4$ Hz, ArH), 8.31 (2H, d, $J = 8.4$ Hz, ArH), 8.48 (2H, d, $J = 8.2$ Hz, ArH), 8.59 (2H, d, $J = 8.2$ Hz, ArH), 8.87 (4H, brm, βH), 8.91 (2H, d, $J = 4.8$ Hz, βH), 8.96 (2H, d, $J = 4.8$ Hz, βH); ^{19}F NMR (400 MHz, 1% Pyridine-*d*5 in CDCl_3): δ -161.96 – -161.78 (4F, m, ArF), -152.16 (2F, t, $J = 21.0$ ArF), -137.03 (4F, dd, $J = 8.0$ Hz, 23.9 Hz, ArF); MALDI-TOF-MS m/z . calcd. for $\text{C}_{47}\text{H}_{22}\text{F}_{10}\text{N}_4\text{O}_4$ 896.148, obsd. 896.153.



Zinc 5-(4-carbomethoxyphenyl)-15-(4-carboxyphenyl)-10,20-bis(pentafluorophenyl)

porphyrin (1). $\text{Zn}(\text{OAc}_2) \cdot 2\text{H}_2\text{O}$ (98 mg, 0.45 mmol) was added to a solution of 5-(4-carbomethoxyphenyl)-15-(4-carboxyphenyl)-10,20-bis(pentafluorophenyl)porphyrin (40 mg, 0.04 mmol) in a mixture of dichloromethane and methanol (80:20, 60 mL). After stirring for 15 h, the solution was diluted with dichloromethane (25 mL) and washed with water (85 mL), then a saturated solution of aqueous sodium bicarbonate. The organic phase was dried over sodium sulfate, filtered, and the solvent evaporated at reduced pressure. The product was purified by column chromatography on silica using 5% methanol in dichloromethane as the eluent to give 42 mg of the desired porphyrin (97% yield). ^1H NMR (500 MHz, 1% Pyridine-*d*5 in CDCl_3): δ 4.10 (3H, s, CO_2CH_3), 8.24 (2H, d, $J = 8.1$ Hz, ArH), 8.25 (2H, d, $J = 8.1$ Hz, ArH), 8.42 (2H, d, $J = 8.1$ Hz, ArH), 8.52 (2H, d, $J = 8.1$ Hz, ArH), 8.87 (4H, brd, $J = 4.6$ Hz, βH), 8.90 (2H, d, $J = 4.6$ Hz, βH); 8.95 (2H, d, $J = 4.6$ Hz, βH); ^{19}F NMR (400 MHz, 1% Pyridine-*d*5 in CDCl_3): δ -162.76 – -162.51 (4F, m, ArF), -153.37 (2F, t, $J = 21.1$ Hz, ArF); -137.51 (4F, dd, $J = 8.3$ Hz, 24.5 Hz, ArF); MALDI-TOF-MS m/z . calcd. for $\text{C}_{47}\text{H}_{20}\text{F}_{10}\text{N}_4\text{O}_4\text{Zn}$ 958.062, obsd. 958.062.



Cp*IrCl(3'-carboxy-2-phenylpyridine) (2). A solution of [Cp*IrCl₂]₂ (300 mg, 0.38 mmol) in dichloromethane (10 mL) was added to a mixture of 3-(pyridin-2-yl)benzoic acid (150 mg, 0.75 mmol) and NaOAc•3H₂O (132 mg, 0.97 mmol) in methanol (10 mL). The mixture was purged with argon, stirred at room temperature for 24 h, filtered twice through celite and the solvent evaporated at reduced pressure. The product was purified by recrystallization from dichloromethane/hexanes (174 mg, 40 % yield). ¹H NMR (500 MHz, CDCl₃): δ 1.62 (15H, s, CH₃), 7.10-7.14 (1H, m, PyrH), 7.66-7.71 (1H, m, PyrH), 7.78 (1H, d, *J* = 7.9 Hz, ArH), 7.85 (1H, d, *J* = 7.9 Hz, ArH), 7.92 (1H, d, *J* = 7.9 Hz, PyrH), 8.31 (1H, s, ArH); 8.66 (1H, d, *J* = 5.7 Hz, PyrH).

S3. Nuclear Magnetic Resonance Spectra:

Figure S1. 500 MHz ¹H NMR spectra and overlaid COSY of 5-(4-carbomethoxyphenyl)-15-(4-carboxyphenyl)-10,20-bis(pentafluorophenyl)porphyrin recorded in 1 % pyridine-*d*₅ in chloroform-*d*.

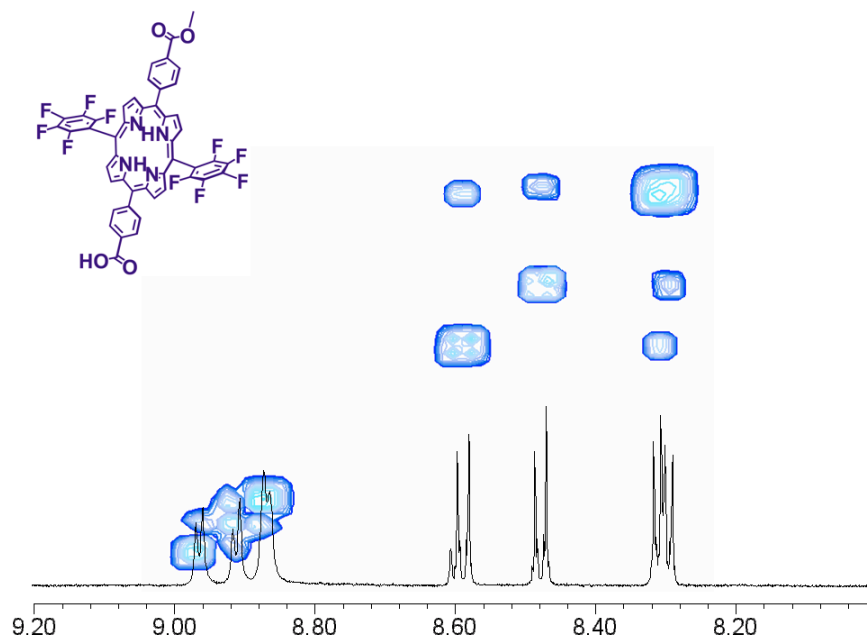


Figure S2. 500 MHz ^1H NMR spectra and overlaid COSY of **1** recorded in 1 % pyridine-*d*5 in chloroform-*d*.

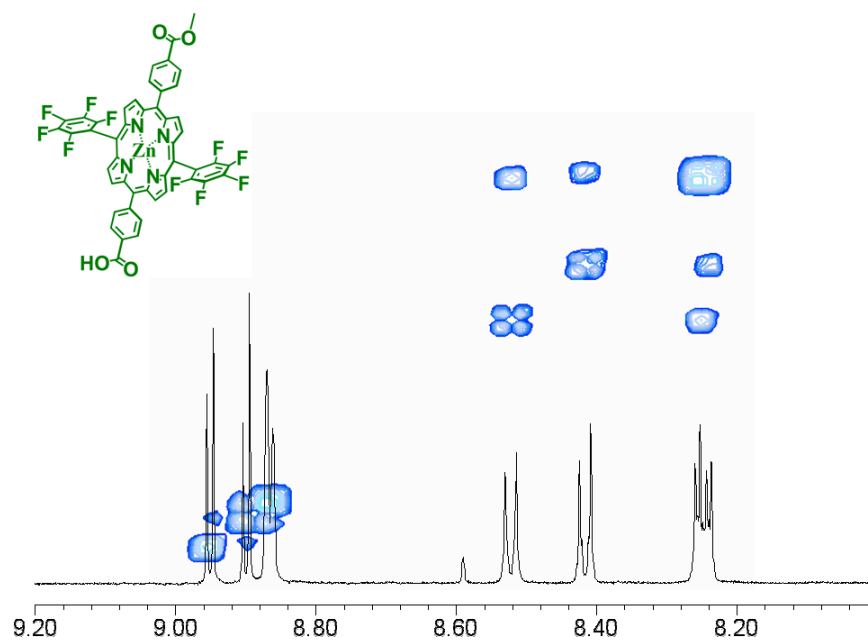


Figure S3. 400 MHz ^{19}F NMR spectra of **1** recorded in 1 % pyridine-*d*5 in chloroform-*d*.

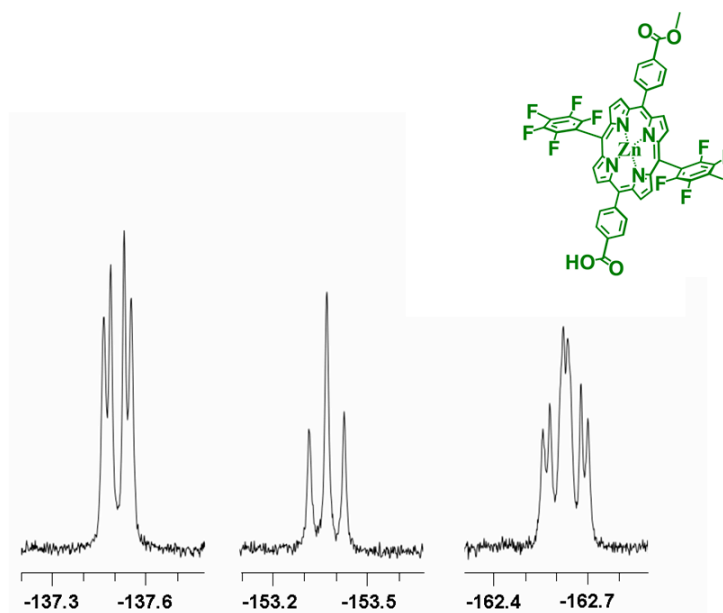
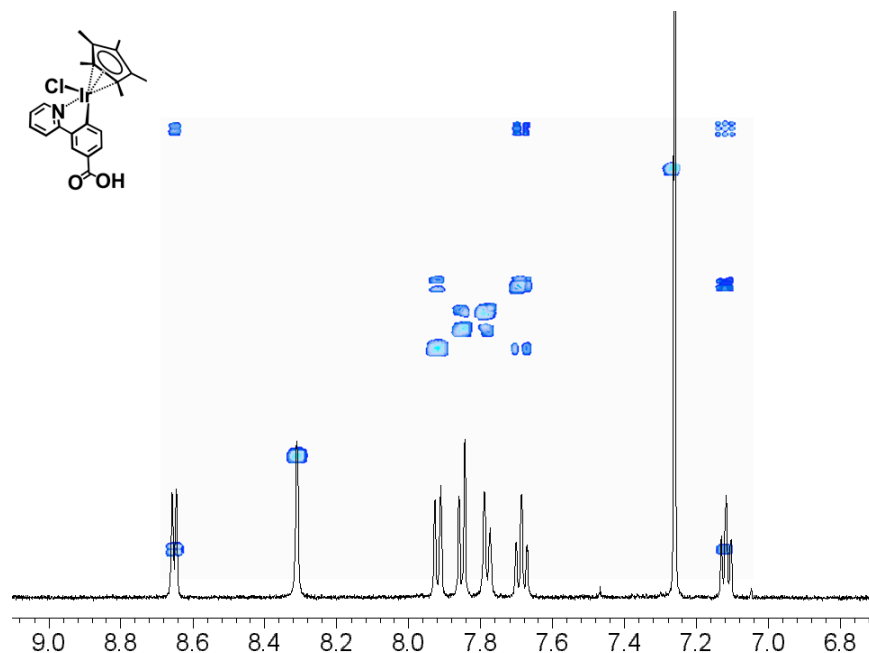


Figure S4. 500 MHz ^1H NMR spectra and overlaid COSY of **2** recorded in chloroform-*d*.



S4. Optical and Electrochemical Data:

Figure S5. Cyclic voltammogram (left) recorded at a glassy carbon electrode as well as the absorption spectrum (right), of 5,15-Bis(4-carbomethoxyphenyl)-10,20-bis(pentafluorophenyl) porphyrin in dichloromethane.

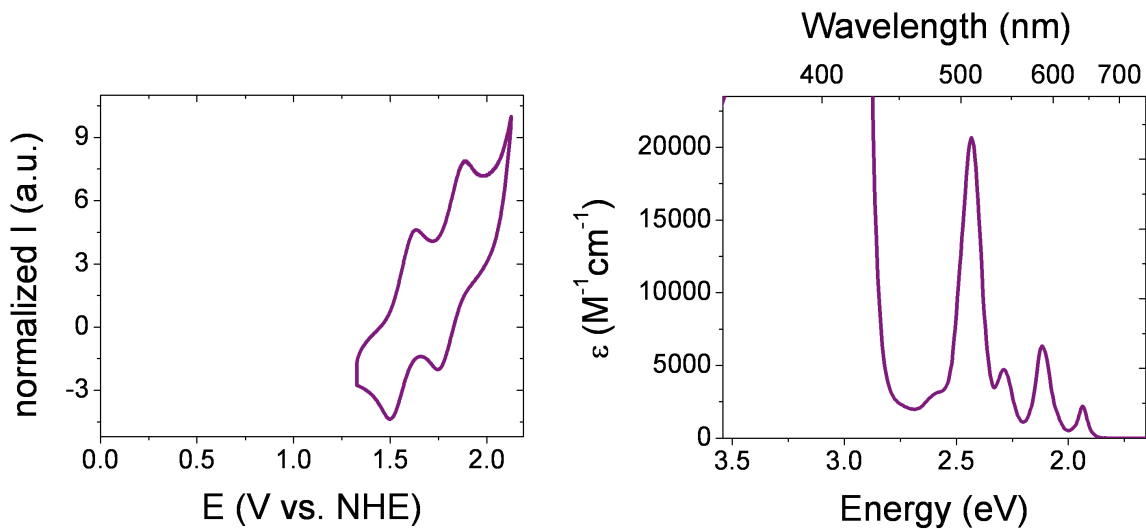


Figure S6. Normalized absorption (solid) and emission (left) spectra of 5,15-Bis(4-carbomethoxyphenyl)-10,20-bis(pentafluorophenyl) porphyrin recorded in dichloromethane, showing the overall spectral profiles (left) as well the intersection of the normalized longest-wavelength absorption and shortest-wavelength emission band, giving an estimated E^{0-0} transition energy of ~ 1.93 eV.

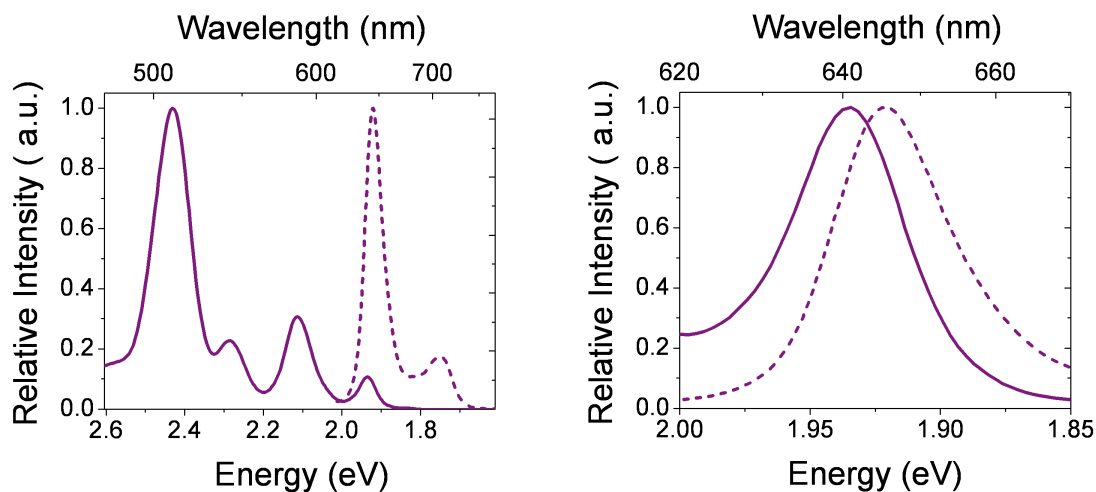


Figure S7. Cyclic voltammograms (left) recorded at a glassy carbon electrode in a dichloromethane solution of the methyl ester of zinc porphyrin **1** (green) and an acetonitrile solution of our unfunctionalized iridium catalyst (black) as well as absorption spectra (right), recorded in a dichloromethane of the methyl ester of zinc porphyrin **1** (green) and the iridium catalyst **2** (black).

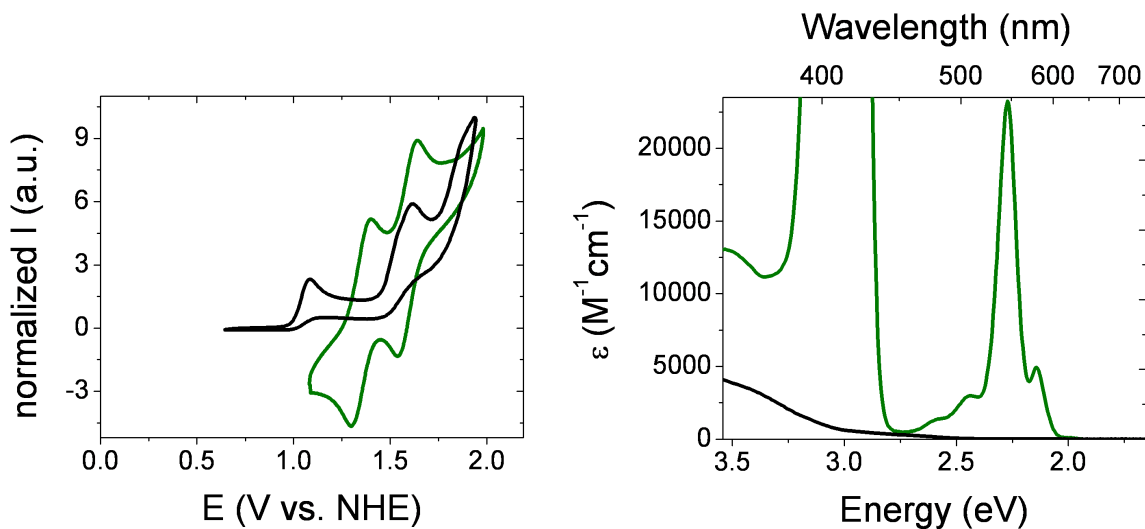


Figure S8. Normalized absorption (solid) and emission (left) spectra of the methyl ester of zinc porphyrin **1** recorded in dichloromethane, showing the overall spectral profiles (left) as well the intersection of the normalized longest-wavelength absorption and shortest-wavelength emission band, giving an estimated E^{0-0} transition energy of ~ 2.12 eV.

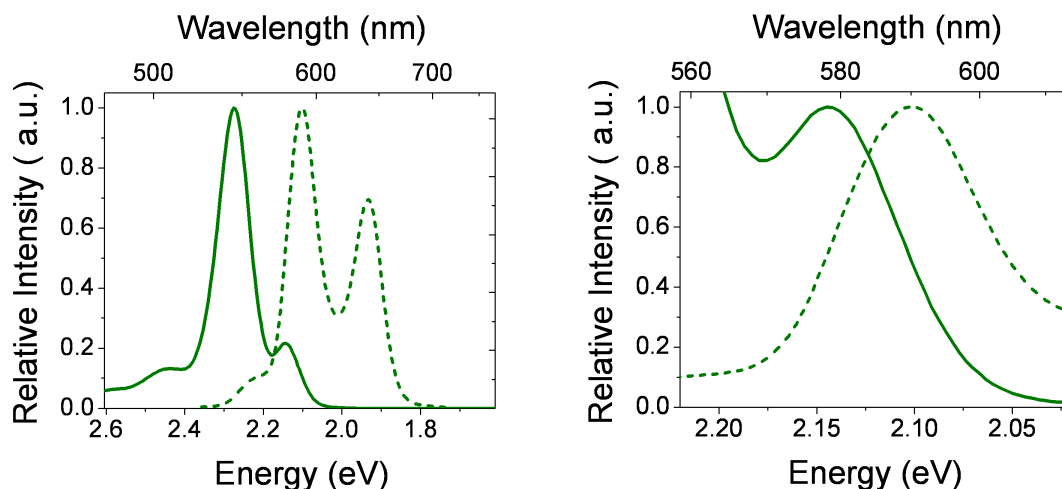


Figure S9. Normalized absorption (green) of the methyl ester of zinc porphyrin **1** recorded in dichloromethane and the diffuse reflectance spectra (dark yellow) of **1-TiO₂** (illustrated in green in Figure 1 of the manuscript). The reflectance spectrum of the immobilized species appears bathochromically shifted in comparison with solution absorption measurements of the model compound, indicating a coupling of the transition moments of the constituent dyes on the surface consistent with J-aggregation.

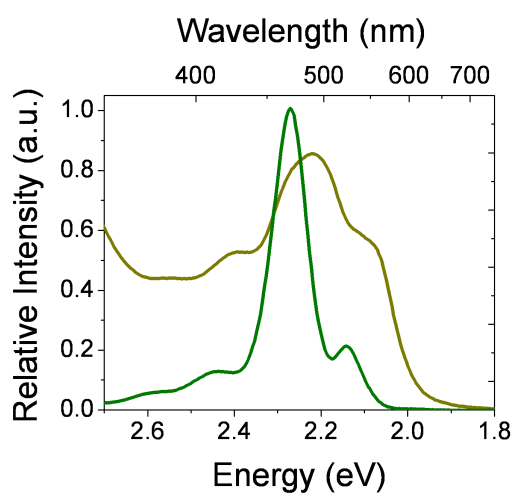
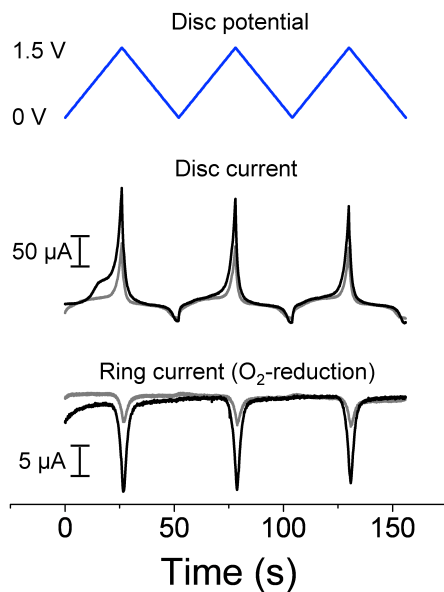
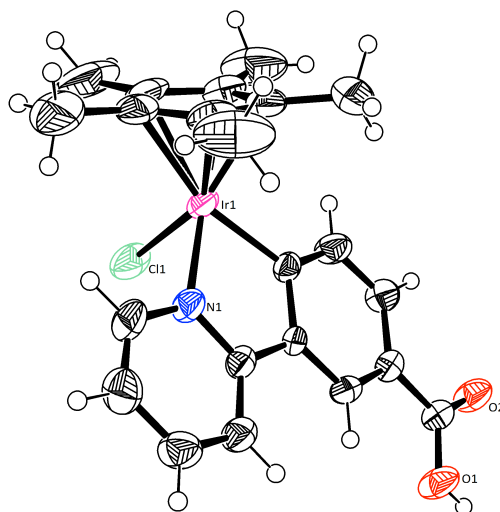


Figure S10. Rotating ring-disk electrode measurements (100 mV/s) of oxygen evolution from a 0.1 M Na_2O_4 aqueous solution using a TiO_2 sintered Pt-disk electrode (grey) and 2-functionalized TiO_2 sintered Pt-disk electrode (black). (top) Disc potential. (middle) Disc current. (bottom) Pt-ring current. (The Pt-ring was held at -0.3 V vs. NHE.)



S5. X-ray Crystal Structure of $\text{Cp}^*\text{IrCl}(3'$ -carboxy-2-phenylpyridine) (2):

Figure S11. X-ray crystal structure of $\text{Cp}^*\text{IrCl}(3'$ -carboxy-2-phenylpyridine) (2)



S5.1. Crystal Data

Empirical Formula	IrCl ₃ O ₂ NC ₂₃ H ₂₅
Formula Weight	646.04
Crystal Color, Habit	yellow, prism
Crystal Dimensions	0.13 X 0.10 X 0.05 mm
Crystal System	monoclinic
Lattice Type	Primitive
Indexing Images	6 images @ 20.0 seconds
Detector Position	49.90 mm
Lattice Parameters	a = 8.2581(8) Å b = 15.3706(14) Å c = 20.2039(18) Å β = 92.606(2)° V = 2561.9(4) Å ³
Space Group	P2 ₁ /n (#14)
Z value	4
D _{calc}	1.675 g/cm ³
F ₀₀₀	1256.00
μ(MoKα)	55.566 cm ⁻¹

S5.2. Intensity Measurements

Diffractometer	Rigaku SCXmini
Radiation	MoKα (λ = 0.71075 Å)
Detector Aperture	75 mm round
Data Images	540 images
Exposure Rate	60.0 sec./°
ω oscillation Range 1 (χ=54.0, φ=0.0)	-120.0 - 60.0°
ω oscillation Range 1 (χ=54.0, φ=120.0)	-120.0 - 60.0°
ω oscillation Range 1 (χ=54.0, φ=240.0)	-120.0 - 60.0°
Detector Swing Angle	-28.40°
Detector Position	49.90 mm
2θ _{max}	55.0°
No. of Reflections Measured	Total: 25141 Unique: 5823 (R _{int} = 0.069)
Corrections	Lorentz-polarization, Absorption (trans. factors: 0.482 - 0.757)

S5.3. Structure Solution and Refinement

Structure Solution	Direct Methods (SIR92)
Refinement	Full-matrix least-squares on F ²
Function Minimized	Σ w (F _o ² - F _c ²) ²
Least Squares Weights	w = 1 / [σ ² (F _o ²) + (0.0337 · P) ² + 2.3179 · P] where P = (Max(F _o ² , 0) + 2F _c ²)/3
2θ _{max} cutoff	55.0°
Anomalous Dispersion	All non-hydrogen atoms
No. Observations (All reflections)	5823
No. Variables	281
Reflection/Parameter Ratio	20.72
Residuals: R1 (I > 2.00σ(I))	0.0469
Residuals: R (All reflections)	0.0783
Residuals: wR2 (All reflections)	0.0900
Goodness of Fit Indicator	1.068
Max Shift/Error in Final Cycle	0.001
Maximum peak in Final Diff. Map	0.87 e ⁻ /Å ³
Minimum peak in Final Diff. Map	-0.68 e ⁻ /Å ³

S5.4. Experimental Details

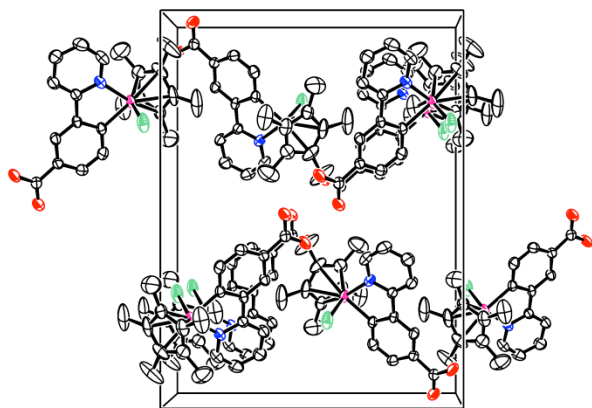
The crystal sample was mounted in a MiTeGen polyimide loop with immersion oil. All measurements were made on a Rigaku Mercury2 CCD area detector with filtered Mo-K α radiation at a temperature of -50°C. The structure was solved by direct methods⁸ and expanded using Fourier techniques.⁹ The non-hydrogen atoms were refined anisotropically. Hydrogen atoms were refined using the riding model. Chlorine atom Cl2 was refined as occupied over two sites of 0.65 and 0.35 occupancy. Cl2 and Cl2' were restrained to have similar thermal parameters using the SADI restraint. Hydrogen atoms H23A and H23B were added as a riding contribution on the higher occupied of the two methylene chloride orientations. The final cycle of full-matrix least-squares refinement (Least Squares function minimized: (SHELXL97) $\sum w(F_o^2 - F_c^2)^2$ where $w = 1/(\sigma^2(F_o^2) + (0.00149P)^2)$ on F^2 was based on 5823 observed reflections and 281 variable parameters and converged (largest parameter shift was 0.00 times its esd) with unweighted and weighted agreement factors of:

$$R1 = \frac{\sum ||F_o| - |F_c||}{\sum |F_o|} = 0.0469$$
$$wR2 = \left[\frac{\sum (w (F_o^2 - F_c^2)^2)}{\sum w(F_o^2)^2} \right]^{1/2} = 0.0900$$

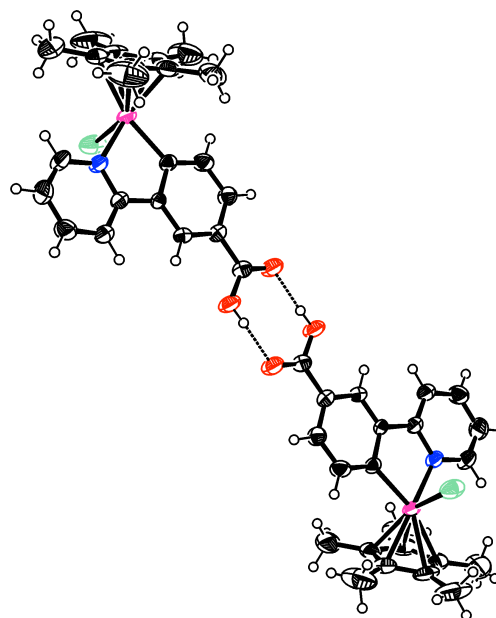
The standard deviation of an observation of unit weight (Standard deviation of an observation of unit weight: $[\sum w(F_o^2 - F_c^2)^2 / (No - Nv)]^{1/2}$ where: No = number of observations, Nv = number of variables) was 1.07. Unit weights were used. The maximum and minimum peaks on the final difference Fourier map corresponded to 0.87 and -0.68 e⁻/Å³, respectively.

Neutral atom scattering factors were taken from Cromer and Waber.¹⁰ Anomalous dispersion effects were included in Fcalc¹¹; the values for $\Delta f'$ and $\Delta f''$ were those of Creagh and McAuley.¹² The values for the mass attenuation coefficients are those of Creagh and Hubbell.¹³ All calculations were performed using the CrystalStructure¹⁴ crystallographic software package except for refinement, which was performed using SHELXL-97.

S5.5. Additional Images



View of packing along a
(H-atoms and solvent omitted)



View of H-bond pair

Table S1. Atomic coordinates and $B_{\text{iso}}/B_{\text{eq}}$

atom	x	y	z	B_{eq}^a
Ir(1)	0.43025(3)	0.601813(14)	0.271956(12)	2.836(7)
Cl(1)	0.6563(2)	0.54669(11)	0.21413(10)	4.83(4)
Cl(2)	0.8433(13)	0.1166(8)	0.5078(4)	20.9(4)
Cl(2')	0.655(5)	0.078(2)	0.4856(13)	35.6(17)
Cl(3)	0.6043(8)	0.2189(6)	0.4340(3)	25.8(3)
O(1)	0.5716(5)	0.9737(2)	0.0840(2)	4.11(9)
O(2)	0.3900(5)	0.9130(2)	0.0130(2)	3.93(9)
N(1)	0.5936(5)	0.6910(3)	0.3162(2)	2.98(9)
C(1)	0.3594(8)	0.5106(5)	0.3529(4)	4.88(17)
C(2)	0.3339(9)	0.4681(4)	0.2904(4)	4.94(17)
C(3)	0.2223(8)	0.5191(4)	0.2504(3)	3.94(13)
C(4)	0.1739(7)	0.5913(4)	0.2890(3)	4.09(14)
C(5)	0.2638(9)	0.5875(4)	0.3510(3)	4.52(15)
C(6)	0.4643(11)	0.4735(7)	0.4089(5)	9.9(3)
C(7)	0.4090(11)	0.3849(4)	0.2690(5)	9.0(3)
C(8)	0.1473(11)	0.4918(6)	0.1845(4)	8.0(2)
C(9)	0.0425(9)	0.6564(5)	0.2678(5)	7.2(2)
C(10)	0.2472(12)	0.6507(6)	0.4069(4)	8.2(2)
C(11)	0.6791(8)	0.6778(4)	0.3741(3)	3.96(13)
C(12)	0.7775(8)	0.7386(4)	0.4029(3)	4.32(14)
C(13)	0.7941(8)	0.8183(4)	0.3723(3)	3.98(13)
C(14)	0.7140(7)	0.8328(3)	0.3114(3)	3.30(12)
C(15)	0.6138(6)	0.7681(3)	0.2845(2)	2.55(10)
C(16)	0.5228(6)	0.7734(3)	0.2202(2)	2.33(9)
C(17)	0.5359(7)	0.8430(3)	0.1766(2)	2.74(10)
C(18)	0.4476(7)	0.8425(3)	0.1160(2)	2.59(10)
C(19)	0.3456(7)	0.7721(3)	0.1007(2)	3.16(11)
C(20)	0.3354(7)	0.7026(3)	0.1434(3)	3.49(12)
C(21)	0.4215(6)	0.7006(3)	0.2045(2)	2.48(9)
C(22)	0.4661(7)	0.9127(3)	0.0668(3)	2.87(10)
C(23)	0.7582(18)	0.1575(15)	0.4391(8)	16.0(6)

Table S2. Atomic coordinates and B_{iso} of hydrogen atoms

atom	x	y	z	B_{iso}
H(1A)	0.5812	1.0081	0.0527	4.95
H(23A)	0.8443	0.1892	0.4176	19.24
H(23B)	0.7315	0.1075	0.4105	19.24
H(6A)	0.5112	0.4190	0.3950	11.83
H(6B)	0.3990	0.4634	0.4469	11.83
H(6C)	0.5503	0.5143	0.4209	11.83
H(7A)	0.5251	0.3926	0.2665	10.86
H(7B)	0.3630	0.3685	0.2257	10.86
H(7C)	0.3874	0.3395	0.3007	10.86
H(8A)	0.0664	0.5342	0.1698	9.58
H(8B)	0.0963	0.4353	0.1888	9.58
H(8C)	0.2306	0.4881	0.1523	9.58
H(9A)	0.0316	0.6994	0.3024	8.69
H(9B)	-0.0598	0.6261	0.2602	8.69
H(9C)	0.0718	0.6850	0.2273	8.69
H(10A)	0.3221	0.6351	0.4433	9.83
H(10B)	0.1372	0.6490	0.4217	9.83
H(10C)	0.2716	0.7090	0.3917	9.83
H(11)	0.6695	0.6238	0.3953	4.75
H(12)	0.8341	0.7267	0.4433	5.18
H(13)	0.8588	0.8620	0.3924	4.77
H(14)	0.7274	0.8856	0.2888	3.96
H(17)	0.6040	0.8902	0.1879	3.28
H(19)	0.2830	0.7722	0.0606	3.79
H(20)	0.2687	0.6553	0.1310	4.19

$$^a B_{\text{eq}} = 8/3 \pi^2 (U_{11}(\text{aa}^*)^2 + U_{22}(\text{bb}^*)^2 + U_{33}(\text{cc}^*)^2 + 2U_{12}(\text{aa}^*\text{bb}^*)\cos \gamma + 2U_{13}(\text{aa}^*\text{cc}^*)\cos \beta + 2U_{23}(\text{bb}^*\text{cc}^*)\cos \alpha)$$

Table S3. Anisotropic displacement parameters^b

atom	U ₁₁	U ₂₂	U ₃₃	U ₁₂	U ₁₃	U ₂₃	Occupancy
Ir(1)	0.03848(14)	0.02497(12)	0.04496(15)	-0.00100(12)	0.00925(10)	0.00848(11)	
Cl(1)	0.0576(11)	0.0343(8)	0.0945(14)	0.0068(7)	0.0347(10)	0.0054(8)	
Cl(2)	0.239(10)	0.390(14)	0.156(6)	-0.006(9)	-0.074(7)	0.026(7)	0.654
Cl(2')	0.56(5)	0.54(4)	0.24(2)	-0.24(4)	-0.00(2)	0.16(2)	0.346
Cl(3)	0.226(6)	0.450(11)	0.296(7)	0.140(7)	-0.082(5)	-0.152(8)	
O(1)	0.071(3)	0.041(2)	0.042(2)	-0.019(2)	-0.012(2)	0.017(2)	
O(2)	0.067(3)	0.040(2)	0.042(2)	-0.012(2)	-0.003(2)	0.0107(19)	
N(1)	0.042(2)	0.034(2)	0.037(2)	-0.000(2)	0.004(2)	0.010(2)	
C(1)	0.046(4)	0.073(5)	0.067(5)	-0.021(4)	0.002(3)	0.037(4)	
C(2)	0.057(4)	0.028(3)	0.106(6)	-0.007(3)	0.038(4)	0.013(3)	
C(3)	0.056(4)	0.040(3)	0.055(4)	-0.019(3)	0.007(3)	0.003(3)	
C(4)	0.038(3)	0.044(4)	0.074(5)	-0.009(3)	0.017(3)	0.009(3)	
C(5)	0.062(4)	0.054(4)	0.058(4)	-0.016(3)	0.027(3)	-0.003(3)	
C(6)	0.092(7)	0.157(10)	0.123(8)	-0.043(7)	-0.021(6)	0.103(8)	
C(7)	0.115(8)	0.034(4)	0.202(12)	-0.012(4)	0.084(8)	0.002(5)	
C(8)	0.111(8)	0.113(7)	0.079(6)	-0.067(6)	-0.004(5)	-0.003(5)	
C(9)	0.041(4)	0.064(5)	0.172(10)	0.001(4)	0.020(5)	0.020(6)	
C(10)	0.114(8)	0.122(8)	0.079(6)	-0.052(7)	0.046(6)	-0.030(6)	
C(11)	0.058(4)	0.044(3)	0.048(4)	0.003(3)	0.001(3)	0.020(3)	
C(12)	0.057(4)	0.064(4)	0.042(3)	0.001(3)	-0.007(3)	0.011(3)	
C(13)	0.053(4)	0.050(4)	0.047(3)	-0.013(3)	-0.006(3)	-0.001(3)	
C(14)	0.046(3)	0.037(3)	0.042(3)	-0.005(2)	-0.002(3)	0.009(2)	
C(15)	0.035(3)	0.029(2)	0.033(3)	0.003(2)	0.006(2)	0.004(2)	
C(16)	0.027(3)	0.022(2)	0.039(3)	0.004(2)	0.001(2)	0.004(2)	
C(17)	0.036(3)	0.028(2)	0.040(3)	-0.006(2)	0.001(2)	0.004(2)	
C(18)	0.039(3)	0.028(2)	0.031(3)	0.003(2)	0.005(2)	0.002(2)	
C(19)	0.046(3)	0.041(3)	0.032(3)	-0.004(2)	-0.002(2)	0.002(2)	
C(20)	0.050(4)	0.034(3)	0.048(3)	-0.012(3)	-0.004(3)	-0.003(2)	
C(21)	0.032(3)	0.024(2)	0.038(3)	0.004(2)	0.007(2)	0.002(2)	
C(22)	0.043(3)	0.030(3)	0.036(3)	-0.003(2)	0.004(2)	0.000(2)	
C(23)	0.109(11)	0.34(2)	0.165(15)	0.010(15)	0.016(11)	0.004(16)	

^b The general temperature factor expression: $\exp(-2\pi^2(a^2U_{11}h^2 + b^2U_{22}k^2 + c^2U_{33}l^2 + 2a*b*U_{12}hk + 2a*c*U_{13}hl + 2b*c*U_{23}kl))$

Table S4. Bond lengths (Å)

atom	atom	distance	atom	atom	distance
Ir(1)	Cl(1)	2.4011(19)	Ir(1)	N(1)	2.094(4)
Ir(1)	C(1)	2.253(8)	Ir(1)	C(2)	2.241(6)
Ir(1)	C(3)	2.165(6)	Ir(1)	C(4)	2.166(6)
Ir(1)	C(5)	2.165(7)	Ir(1)	C(21)	2.040(5)
Cl(2)	C(23)	1.653(19)	O(1)	C(22)	1.315(7)
O(2)	C(22)	1.231(7)	N(1)	C(11)	1.353(7)
N(1)	C(15)	1.361(7)	C(1)	C(2)	1.429(11)
C(1)	C(5)	1.421(10)	C(1)	C(6)	1.505(12)
C(2)	C(3)	1.432(10)	C(2)	C(7)	1.495(10)
C(3)	C(4)	1.425(9)	C(3)	C(8)	1.503(11)
C(4)	C(5)	1.428(10)	C(4)	C(9)	1.523(10)
C(5)	C(10)	1.500(12)	C(11)	C(12)	1.353(9)
C(12)	C(13)	1.381(9)	C(13)	C(14)	1.388(8)
C(14)	C(15)	1.389(8)	C(15)	C(16)	1.473(7)
C(16)	C(17)	1.394(7)	C(16)	C(21)	1.424(7)
C(17)	C(18)	1.395(7)	C(18)	C(19)	1.398(8)
C(18)	C(22)	1.481(7)	C(19)	C(20)	1.378(8)
C(20)	C(21)	1.397(8)			

S.6. References:

1. G. Li, C. P. Richter, R. L. Milot, L. Cai, C. A. Schmuttenmaer, R. H. Crabtree, G. W. Brudvig and V. S. Batista, *Dalton Transactions*, 2009, 10078-10085.
 2. D. T. Sawyer, A. Sobkowiak and J. L. Roberts, *Electrochemistry for Chemists*, 2nd edn., Wiley, New York, 1995.
 3. A. J. Bard and L. R. Faulkner, *Electrochemical Methods: Fundamentals and Applications*, 2nd edn., Hoboken, 2001.
 4. M. C. Beard, G. M. Turner and C. A. Schmuttenmaer, *Physical Review B: Condensed Matter and Materials Physics*, 2000, 62, 15764-15777.
 5. J. B. Baxter and C. A. Schmuttenmaer, *Journal of Physical Chemistry B*, 2006, 110, 25229-25239.
 6. G. M. Turner, M. C. Beard and C. A. Schmuttenmaer, *Journal of Physical Chemistry B*, 2002, 106, 11716-11719.
 7. C.-H. Lee and J. S. Lindsey, *Tetrahedron* 1994, 50, 11427-11440.
 8. G. M. Sheldrick, *Acta Cryst.*, 2008, A64, 112-122.
 9. P. T. Beurskens, G. Admiraal, G. Beurskens, W. P. Bosman, R. de Gelder, R. Israel and J. M. M. T. Smits, *The DIRDIF-99 program system*, University of Nijmegen, The Netherlands, 1999.
 10. D. T. Cromer and J. T. Waber, The Kynoch Press, Birmingham, England, 1974, Table 2.2 A.
 11. J. A. Ibers and W. C. Hamilton, *Acta Cryst.*, 1964, 17, 781.
 12. D. C. Creagh and W. J. McAuley, Kluwer Academic Publishers, Boston, 1992, Table 4.2.6.8, pages 219-222.
 13. D. C. Creagh and J. H. Hubbell, Kluwer Academic Publishers, Boston, 1992, Table 4.2.4.3, pages 200-206.
 14. *CrystalStructure 3.8: Crystal Structure Analysis Package*, (2000-2007) Rigaku Rigaku Americas 9009 New Trails Dr. The Woodlands TX 77381 USA.
-